

# Plasma Structure Decay Rates in the Equatorial Ionosphere are Strongly Coupled by Turbulence

M F Ivarsen<sup>1,2</sup>, J-P St-Maurice<sup>2,3</sup>, J Park<sup>4,5</sup>, J Klenzing J<sup>6</sup>, Y Jin<sup>1</sup>, and W Lee<sup>4,5</sup>

<sup>1</sup>Department of Physics, University of Oslo, Oslo, Norway

<sup>2</sup>Department of Physics and Engineering Physics, University of Saskatchewan, Saskatoon, Saskatchewan, Canada

<sup>4</sup>Korea Astronomy and Space Science Institute, Daejeon, South Korea

<sup>5</sup>Department of Astronomy and Space Science, Korea University of Science and Technology, Daejeon, South Korea

<sup>3</sup>Department of Physics and Astronomy, University of Western Ontario, London, Ontario, Canada

<sup>6</sup>Goddard Space Flight Center, National Aeronautics and Space Administration, Greenbelt, MD, United States

## Key Points:

- Turbulence forces equatorial irregularities to decay with a scale-independent rate
- Equatorial irregularities of scale-sizes between 500 m and 75 km are not dissipating by chemical recombination or perfect ambipolar diffusion
- Equatorial plasma irregularities exhibit a characteristic decay time of approximately 1.4 hours

---

Corresponding author: Magnus F Ivarsen, [m.f.ivarsen@fys.uio.no](mailto:m.f.ivarsen@fys.uio.no)

## Abstract

Equatorial plasma irregularities in the ionospheric F-region proliferate after sunset, causing the most apparent radio scintillation “hot-spot” in geospace. These irregularities are caused by plasma instabilities, and appear mostly in the form of under-densities that rise up from the F-region’s bottomside. After an irregularity production peak at sunset, the amplitude of the resulting turbulence decays with time. Analyzing a large database of plasma irregularity spectra observed by one of the European Space Agency’s Swarm satellites, we have applied a novel but conceptually simple statistical analysis to the data, finding in the process that post-sunset turbulence in the F-region tends to decay with a uniform, scale-independent rate at night, thereby confirming and extending the results from earlier case studies. Our results should be of utility for large-scale space weather modelling efforts that are unable to resolve turbulent effects.

## 1 Introduction

The equatorial ionosphere is an area of our Earth’s space environment where the geomagnetic field is nearly horizontal and is, as a result, the birthplace of several interesting electro-hydrodynamic instabilities after sunset. These emerge from the large-scale generalized Rayleigh-Taylor instability (Kelley, 1989). In the evening sector of the topside F-region, localized depletions, or ‘bubbles’, of plasma are therefore routinely observed (Woodman & Hoz, 1976; Heelis, 2004; Kil, 2015). Having formed in the bottomside F-region, large scale bubbles evolve non-linearly while rising upward (Kil & Heelis, 1998; Eccles et al., 2015). Smaller scale structures are then seen to proliferate on the edges of said bubbles, where steep plasma gradients create favorable conditions for irregularity production (Hysell & Kudeki, 2004). Alongside the depletions, *enhancements*, or ‘blobs’, also exist in the topside F-region equatorial ionosphere. Like bubbles, blobs are also located in the evening sector and, like bubbles, carry with them plasma irregularities over a wide range of scales (Oya et al., 1986; Park et al., 2003; Le et al., 2003). At the smaller scales, such irregularities in plasma density cause signal refraction and hence scintillation in satellite communication transmissions (Yeh & Liu, 1982; Basu & Basu, 1985).

The dataset used in the present study is a collection of *in-situ* observations of equatorial plasma bubbles and attendant smaller-scale equatorial irregularities. We make no distinction between clearly recognizable bubbles, blobs, or turbulent plasma observations in general. The useful data are a collection of irregularity spectra, which themselves are Fourier components belonging to turbulent plasma processes. We subject these spectra to a conceptually simple statistical analysis; we aggregate spectral power across 128 frequencies, binned by solar local time (LT) at the time of observation.

By definition, a power spectrum quantifies the distribution of fluctuation power across the (temporal or spatial) scales in which the sampled quantity fluctuates (Stoica & Moses, 2005). Exploiting this quality, PSD analysis is frequently applied to in-situ ionospheric observations of plasma density bubbles (Kelley et al., 1982; Rino et al., 2016), high-latitude turbulence (Mounir et al., 1991), as well as in the larger plasma environment of Earth (Borovsky, 2012). The PSD of ionospheric plasma irregularities is often approximated by a power law of the form

$$P(f) \propto f^{-\eta}, \quad (1)$$

where  $\eta$  is a real-valued exponent, referred to as the spectral index, and  $f$  represents frequency (convertible to spatial wavenumber by an assumption of stationary plasma from the spacecraft point of view). The exponent  $\eta$  has been the subject of many studies of equatorial plasma irregularities (e.g., Dyson et al., 1974; Rino et al., 1981; Kelley & McClure, 1981; Kil & Heelis, 1998). Steepening of this spectral index is proportional to the decay in fluctuation power with increasing wavenumber, and has been characterized in equatorial plasma numerous times in the literature (e.g., LaBelle et al., 1986; Hysell et al., 1994). The decay rate as a function of wavenumber is a manifestation of the active

70 nonlinear distribution of power between wavenumbers, whose nature is a key property  
71 of turbulence (Kolmogorov, 1941).

72 Structured plasmas produce a signal in *in-situ* density time-series. Into this tur-  
73 bulent signal is embedded various forms of non-linear wavenumber interactions. It is not  
74 just influenced by the power growth from plasma instabilities, but can also describe ir-  
75 regularity dissipation (Vickrey & Kelley, 1982; Mounir et al., 1991; Ivarsen et al., 2019).  
76 For instance, dissipation due to ambipolar diffusion has been inferred to cause observ-  
77 able spectral steepening (Kivanc & Heelis, 1998; Ivarsen, St-Maurice, et al., 2021), where  
78 power decreases markedly with increasing wavenumber below some critical scale.

79 Owing to diffusive processes, plasma irregularity dissipation is invariably associ-  
80 ated with a characteristic *structure lifetime*, which quantifies the ensuing temporal ex-  
81ponential decay (Vickrey & Kelley, 1982; Ivarsen, Jin, et al., 2021). A study by Hysell  
82and Kelley (1997) investigated the structure lifetimes of decaying equatorial plasma ir-  
83regularities around local midnight. The authors examined two consecutive orbits made  
84by the AE-E satellite, which had a very low orbital inclination, at times enabling it to  
85effectively orbit along the magnetic equator. The two orbits in question fortuitously did  
86so, observing roughly the same plasma structures on both orbits. The authors exploited  
87this fact to examine the decay in power across a range of wavevectors, during the course  
88of 101 minutes. Hysell and Kelley (1997) found all wavevectors between 80 m and 64 km  
89to decay at roughly the same rate, exhibiting a plasma structure lifetime around 1.4 hour.

90 A study contemporary to the previously mentioned, Kil and Heelis (1998) likewise  
91investigated the temporal evolution of equatorial F-region plasma, also using data from  
92the AE-E satellite. The authors of that study applied power spectral density analysis  
93to the *in-situ* density measurements, and made a statistical foray into the spectral in-  
94dices, or slopes, of the measured irregularity spectra. Kil and Heelis (1998) found that  
95small-scale irregularities grow rapidly around sunset, before decaying shortly thereafter.  
96The authors did not explicitly show a scale-independent decay of power, but concluded  
97that power decays across all wavevectors around local midnight.

98 In the present study, we perform a simple but intriguing statistical analysis of equa-  
99torial F-region plasma irregularities, measured by a Swarm satellite. We sort turbulent  
100spectra by the solar local time of their observation and examine the decay in power with  
101increasing LT. Earth’s rotation is the cause of this diurnal variable, and we consider it  
102to simply denote the passage of time in a co-rotating frame. By fitting exponential curves  
103to PSD as a function of LT, we estimate the *e*-folding time of decaying density irregu-  
104larities at night in the equatorial region.

## 105 2 Methodology

106 The Swarm mission consists of three polar-orbiting satellites with a very high in-  
107clination (Friis-Christensen et al., 2006). This means that the satellites’ orbits are pri-  
108marily oriented north-south geographically, and the orbits can thus be perpendicular to  
109the magnetic equator. In Figure 1a) we show the orbit of Swarm A at around 00:55 UT  
110on 25 October 2014, in a plot showing magnetic latitude on the *y*-axis (using the Solar  
111Magnetic coordinate system Hapgood, 1992) and LT along the *x*-axis. The *geographic*  
112equator is shown with a blue line, while a shaded gray region shows the dark ionosphere  
113at an altitude of 110 km.

114 As alluded to, at the equator the angle between the spacecraft trajectory and Earth’s  
115magnetic field lines can be parallel for a polar orbiting satellite. It is, however, usually  
116oblique (see, e.g., Nakanishi et al., 2014, Figure 13). We must nevertheless consider this  
117angle explicitly, and so we shall denote it by  $\alpha$ ; the full 3D angle between a vector point-  
118ing along the spacecraft trajectory and that of Earth’s magnetic field, the latter estimated  
119using the IGRF model (Alken et al., 2021). Figure 2a–b) illustrates the situation; when

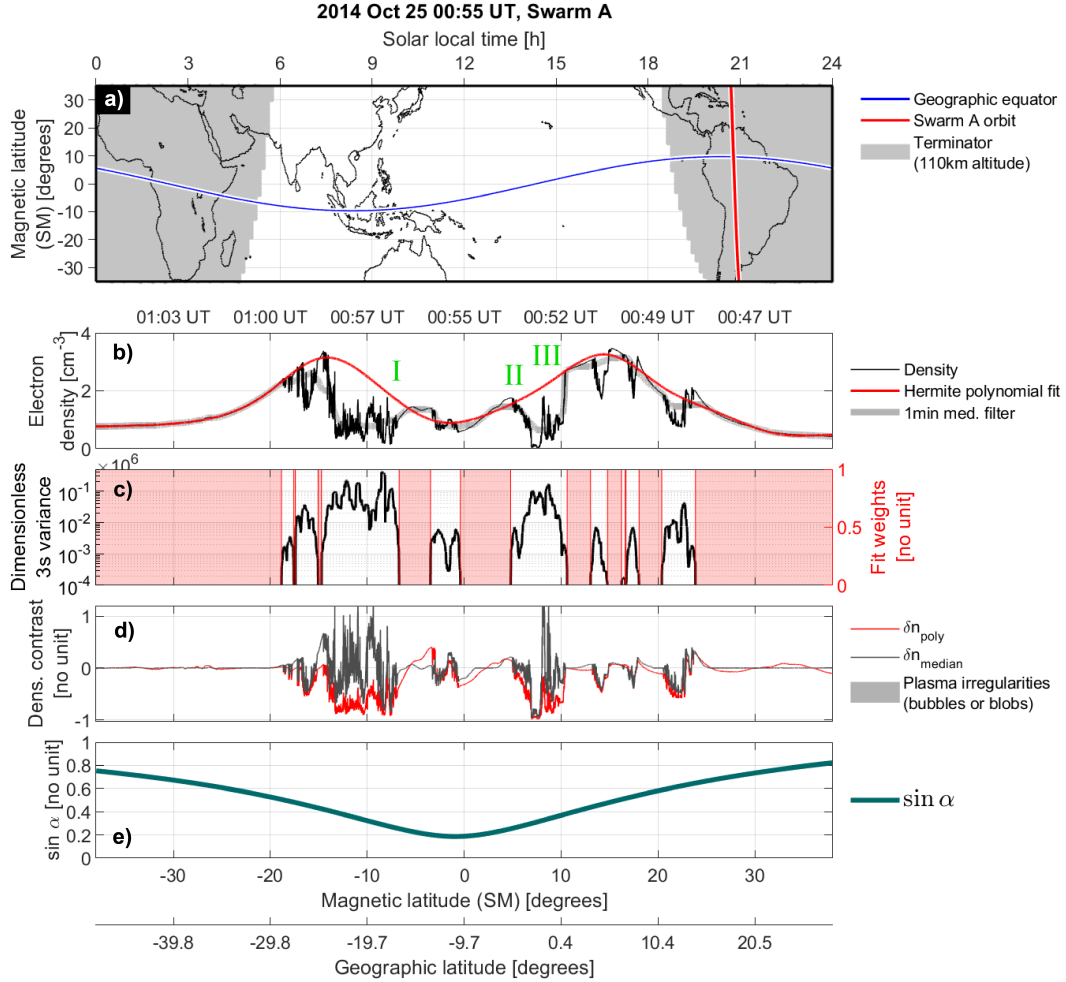


**Figure 1.** 25 October 2014, around 01:00 UT, Swarm A crossed the equator. Panel a) shows the orbit in local time ( $x$ ) magnetic latitude ( $y$ ) coordinates in red line, with the geographic equator in blue line. A shaded grey region indicates darkness in the E-region. Panel b) shows the observed plasma density (black), a Hermite polynomial fit (red), and a one-minute median filter applied to the density (grey). Panel c) shows the 3-second density variance in black, and the resulting fit weights (0 or 1) in shaded red area. The relative plasma density fluctuations  $\delta n$  is shown in gray and red line in Panel d). The angle between spacecraft velocity vector and Earth’s magnetic field is shown in dark green line in panel e). The geographic and geomagnetic latitudes of the orbit are displayed on two  $x$ -axes below panel e). The three Roman numerals posted in panel b) refer to the panels of Figure 2.

120  $\alpha > 0$  the spacecraft velocity  $v_{sc}$  can be decomposed into a field-parallel ( $v_{\parallel}$ ) and field-  
 121 perpendicular ( $v_{\perp}$ ) component. We assume the structures to be strongly magnetic field-  
 122 aligned and therefore ignore the former while expressing the latter as

$$v_{\perp} = v_{sc} \sin \alpha. \quad (2)$$

123 Consequently, the rate at which the spacecraft traverses plasma *field-perpendicularly* gives  
 124 the  $\alpha$ -adjusted perpendicular scale size,

$$L_{\perp} = \frac{v_{sc} \sin \alpha}{f}, \quad (3)$$

125 where  $f$  denotes sampling frequency. Figure 2c plots  $L_{\perp}$  for three selected frequencies.  
 126 As  $\sin \alpha$  approaches zero (orbit parallel to Earth's magnetic field lines)  $L_{\perp}$  gets arbitrar-  
 127 ily small, and the spacecraft runs the risk of resolving temporal waves, nullifying the hy-  
 128 pothesis of plasma being stationary with respect to the spacecraft. We impose a thresh-  
 129 old value of  $\alpha$  that it must make an angle greater than  $10^{\circ}$  against Earth's magnetic field,  
 130 which corresponds to  $v_{\perp} \approx 1.3$  km/s. This threshold can also protect our results from  
 131 the artefacts reported by Song et al. (2022).

132 It follows that when  $\alpha$  is relatively small (but not too small) an orbiting spacecraft  
 133 will effectively sample field-perpendicular irregularities at much smaller scale-sizes than  
 134 the nominal sampling frequency would imply. The effective sampling frequency then be-  
 135 comes,

$$f_{\alpha} = \frac{f}{\sin \alpha}. \quad (4)$$

136 The consequences of this effective mapping between sampling frequency and *in-situ* spa-  
 137 tial scale are understudied, but similar calculations were proposed by Kelley et al. (2003).  
 138 The topic deserves to be revisited in a future paper.

139 The central observable used in the present study is the plasma density,  $n(t)$ , from  
 140 the Advanced Plasma Density by the EFI instrument (Knudsen et al., 2017). With a sam-  
 141 pling rate of 16 Hz (yielding a Nyquist frequency of 8 Hz). With Eq. (4), the effective  
 142 Nyquist frequency becomes 16 Hz when  $\alpha = 30^{\circ}$  – the average value of  $\alpha$  in our dataset.  
 143 The smallest field-perpendicular scale-sizes available in the data are consequently reduced  
 144 to just under 500 m (see Figure S1 in the Supporting Information).

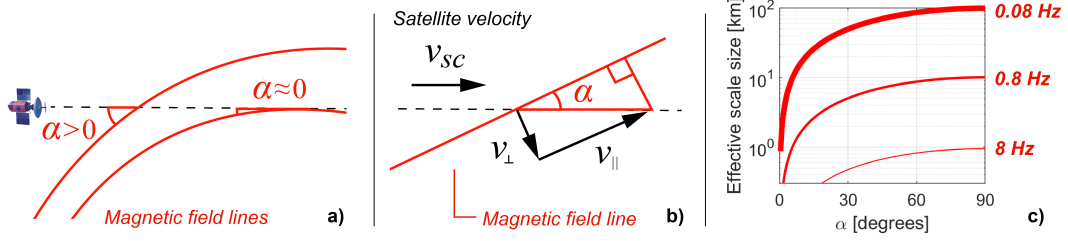
145 As is standard in many studies of plasma irregularities, we likewise quantify the  
 146 *relative* fluctuations in density,

$$\delta n(t) = \frac{n(t)}{\bar{n}(t)} - 1, \quad (5)$$

147 where  $\bar{n}(t)$  represents the ambient (undisturbed) density. We estimate  $\bar{n}(t)$  using two tech-  
 148 niques. One is by fitting a Hermite polynomial to the slowly varying equatorial plasma  
 149 density, applying the reciprocal moving 3-second variance as weights in the fitting scheme.  
 150 This way, orbital segments where the variance is high (implying the presence of irreg-  
 151 ularities) are not considered as representative of the ambient density. Second, as a more  
 152 conventional way of calculating the density contrast, we estimate  $\bar{n}(t)$  using a simple mov-  
 153 ing one-minute median filter.

154 To witness the two methods in action, see panel b) of Figure 1. Here, we show in  
 155 thin black line the measured density, while a one-minute median filter is shown through  
 156 a thick gray line, and the Hermite polynomial is shown with a red line. A density fluc-  
 157 tuation time-series (Eq. 5) can consequently be constructed by division by one of the two  
 158 estimated background density estimates. This being stated, while the Hermite polyno-  
 159 mial evidently succeeds in building a slowly moving ambient density devoid of distur-  
 160 bances, neither method can provide a reliable ambient density inside bubble – that would  
 161 require the measurement of a plasma density that no longer exists.

## Spacecraft magnetic aspect angle



## Plasma irregularity spectra

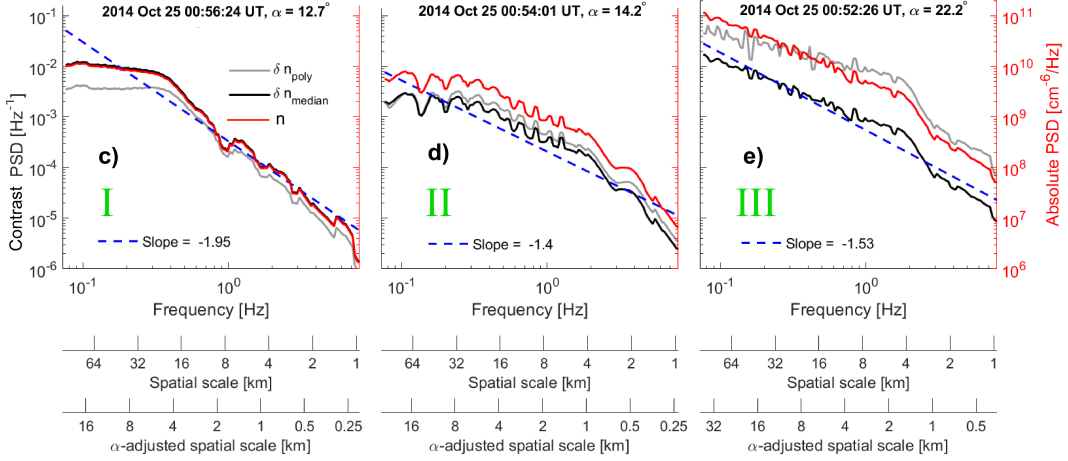


**Figure 2.** Panel a): the geometry of a spacecraft orbiting obliquely against Earth’s magnetic field lines near the magnetic equator, making an angle  $\alpha$  against the field-line. Panel b): the spacecraft velocity vector ( $v_{sc}$ ), and its field-parallel and field-perpendicular components ( $v_{\parallel}$  and  $v_{\perp}$ ). Note that even though the sketch is 2-dimensional, we explicitly calculate the full 3D-angle. Panel c): Eq. (3) for three selected frequencies, as a function of  $\alpha$ . Panels c–d) show example irregularity spectra that are subject to a statistical analysis in the present paper. The three panels show spectra calculated at denoted by green Roman numerals in Figure 1. The two density contrast spectra are shown in black and gray, while an absolute density spectrum is shown in red. Nominal and  $\alpha$ -adjusted spatial scale (Eq. 3) are indicated along the two lower  $x$ -axes.

162 The relative plasma density fluctuations  $\delta n$  are shown in Figure 1d), a dark gray  
 163 line representing the result of using a one-minute median filter, while a red line represents  
 164 the result of using the Hermite polynomial to approach the relative fluctuations.  
 165 We subjected these two time-series (as well as the absolute density) to a running PSD  
 166 analysis with a cadence of 1 s. Each spectrum uses one minute segments, meaning that  
 167 we calculate irregularity spectra with considerable overlap. After applying a Hann win-  
 168 dows to each 60 s segment, we computed averaged periodograms to calculate a logarith-  
 169 mically spaced PSD at 128 frequencies (Tröbs & Heinzel, 2006). This procedure is de-  
 170 scribed in detail in Ivarsen, Jin, et al. (2021) and Ivarsen, St-Maurice, et al. (2021).

171 In Figure 2c–d) we show three sample spectra, calculated for the time-stamps marked  
 172 with green Roman numerals in Figure 1b). We plot power spectral density against sam-  
 173 pling frequency, with the relative density (contrast) spectra in terms of the median smooth-  
 174 ing in black and the polynomial smoothing in gray (left  $y$ -axis). The absolute density  
 175 spectrum is shown in red (right  $y$ -axis), in each panel. The lower  $x$ -axes give the con-

176 ventional inferred scale size ( $L = v_{sc}/f$ ), as well as the  $\alpha$ -adjusted scale size (Eq. 3).  
 177 The value of  $\alpha$  as measured for each spectrum is indicated. We observe that all three  
 178 spectra (black, grey, and red) agree appreciably, with slight variations in slope that are  
 179 attributable to their difference in metric. In what follows, we aggregate some 2 million  
 180 spectra such as those presented in Figure 2c–d), which are systematically classified ac-  
 181 cording to the methods outlined above. In addition to the mentioned  $\alpha$ -criterium, ad-  
 182 ditional criteria for an irregularity spectrum to be identified and calculated include that  
 183  $|\delta n|$  should be greater than at least 5 %, that the running 6 s density fluctuations vari-  
 184 ance should exceed  $10^4$ , and the absolute density should exceed  $5000 \text{ cm}^{-3}$ .

### 185 3 Results

186 We processed an aggregate of some 25,000 equatorial night-time crossings made by  
 187 Swarm A between 2014 and 2022, with the majority of the observations being made prior  
 188 to 2020. Swarm B was excluded, as it is orbiting around at an altitude 50 km higher than  
 189 Swarm A (around one scale height), and we excluded Swarm C, as that satellite orbits  
 190 in tandem with Swarm A, and may observe largely the same structures as Swarm A. Based  
 191 on the 25,000 selected orbits, we identified some 2 million irregularity spectra with the  
 192 method outlined in the previous section. We then binned all observations by LT and by  
 193 effective frequency (Eq. 4) to create composite information about the irregularities and  
 194 their spectra.

195 Panels a) and b) in Figure 3 show the overall absolute density variance,  $\sigma_{RMS}$ , and  
 196 the distribution of irregularity spectra respectively, with both quantities binned by  
 197 LT. In Panel b), we observe a steady rise in irregularity occurrence towards 04h, con-  
 198 trary to the maximum growth rates which peak just after sunset. The reason for this 04h  
 199 peak is that bubbles tend to break up and spread out over a larger region of space as  
 200 they decay, causing a larger number of spectra to be flagged as irregularities post-midnight  
 201 compared to pre-midnight (see Figure S2 in the Supporting Information for a typical post-  
 202 midnight crossing of the equator).

203 In panel a) of Figure 3, a straight green line shows the result of an exponential fit  
 204 of the form

$$\sigma_{RMS} = \sigma_0 e^{-2t/\tau}, \quad (6)$$

205 where  $\sigma_0$  and  $\tau$  are (positive) fitting parameters calculated through a linear least-squares  
 206 minimization applied to the logarithm of the median values, and  $t$  is the solar local time.  
 207 We should mention here that equatorial F-region plasma tends to exhibit a horizontal  
 208 west-east drift velocity (Purslow, 1958; Skinner et al., 1958). However, this drift does  
 209 not show significant variations with respect to solar cycle, geomagnetic activity, or sea-  
 210 son (Woodman, 1972; Fejer et al., 1981). In Figure 3 (and the next figure to come) we  
 211 could adjust the local times by the effect of this west-east plasma drift, but the correc-  
 212 tion has minimal impact on the results, and we abstain from making the adjustment.

213 The decay parameter  $\tau = 1.52 \pm 0.27$  hours in Figure 3a), with error margins  
 214 denoting the 95-percentile confidence interval (3-sigma) of the fit, indicate the  $e$ -folding  
 215 time of the  $\sigma_{RMS}$  quantity with respect to LT, assuming an exponential decay in plasma  
 216 irregularity amplitude after the sunset production peak. This value is consistent with  
 217 the 1.4 h decay rate found by Hysell and Kelley (1997). Moreover, it is, as we shall demon-  
 218 strate, largely independent of irregularity scale size. This decay rate is likewise relatively  
 219 stable across different seasons (not shown), but displays a moderate dependency on ge-  
 220 omagnetic activity, with geomagnetically disturbed conditions being associated with a  
 221 slower decay until around 02h LT (see Figure S4 in the Supporting Information).

222 The rest of the panels in Figure 3 show the same binning procedure used for  $\sigma_{RMS}$   
 223 applied this time to the power spectral density in 16 selected  $\alpha$ -adjusted frequencies be-  
 224 tween 0.2 Hz and 16 Hz (the effective Nyquist frequency, see Figure S1 in the Support-

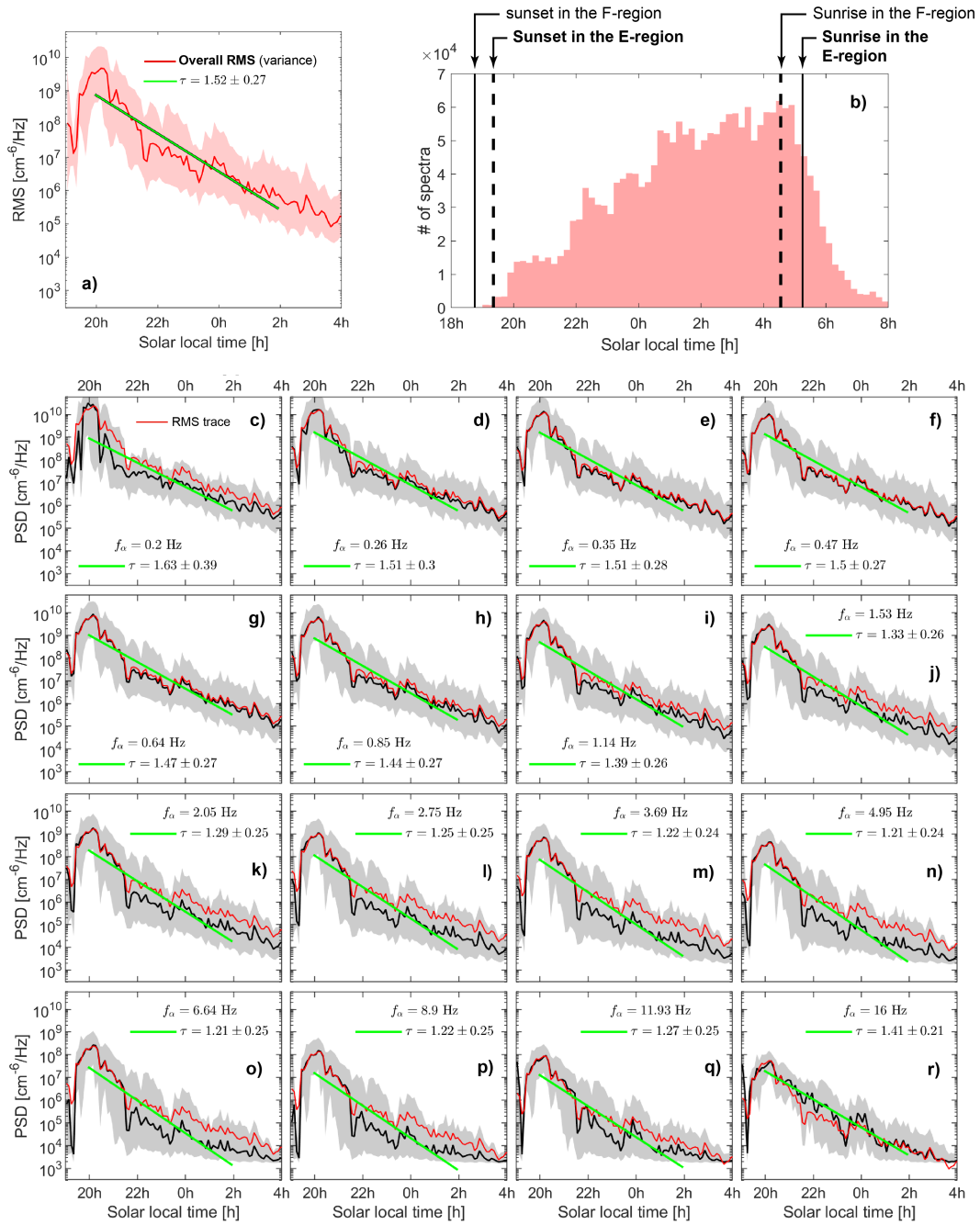


**Figure 3.** Overall absolute density variance (RMS) binned by solar local time (panel a). Number of spectra observed per local time bin, with various solar terminators indicated (panel b). Binned median power across 16 frequencies, with frequency indicated (panels c–r). Each of the 16 panels shows median PSD in black (shaded gray region showing upper- and lower- quartile distributions), with the trace of the overall RMS data shown in a thin red line. Exponential fits (Eq. 6) are shown in green, with structure lifetimes  $\tau$  indicated. For a version of this figure based on relative density (contrast) spectra, see the Figure S3 in the Supporting Information.

ing Information). Panels c-r) of Figure 3 consequently show the median power in each local time bin (with a gray shaded area indicating upper- and lower- quartile distributions). A thin red line gives the trace of the overall RMS curve, multiplied by a constant number that changes with increasing frequency. That constant is selected so as to equalize the area under the  $\sigma_{RMS}$ - and the PSD-curve, leaving the shape of the shifted curve intact.

The agreement between the shifted  $\sigma_{RMS}$  and the PSD is remarkable between 0.26 Hz and 0.85, which happens to be where most of the wave energy is found. This is no accident in view of the following construct, where we Fourier analyze the variations in  $n_i$  when considering the RMS variations:

$$\sigma_{RMS}^2 = \frac{1}{N} \sum_{i=1}^N [n_i(x_i) - \overline{n(\bar{x})}]^2 = \frac{1}{N} \left[ n_0 - \overline{n(\bar{x})} + \sum_{k>0} n_k \cos(kx_i) \right]^2 \approx \frac{1}{2} \frac{\sum_{k>0} n_k^2}{N} \quad (7)$$

In these expressions, we take  $N$   $x_i$ -samples (duration, 1 minute) and explicitly state that the average density is taken over the average  $x$  value for the interval. Secondly, we drop temporal variations, as explained in Section 2. We then assume that the  $k = 0$  term in the Fourier series is equal to  $\bar{n}$ . Finally, we assume that the cosine terms oscillate strongly over the interval so that we replace the sum of the cosines by 0 and the sum of the squares of the cosines by 1/2. Thus, if the dominant wave-numbers all decrease in the same way as a function of LT, the RMS must mimic this decrease. This has to mean that, statistically speaking, the dominant wave numbers obey Eq. (1) with a single exponent  $\eta$  at all LT.

To estimate the decay individually for each  $\alpha$ -adjusted frequency, and prove the above conjecture, we present the result of a fit through Eq. (6) for the PSD as a function of LT, for each individual frequency  $f_\alpha$ . In Figure 3,  $\tau$ , a value twice the  $e$ -folding time, is indicated in each panel. Note that while Figure 3 uses absolute density spectra, we have also repeated the procedure with the density contrast data, with similar results (see Figure S3 in the Supporting Information and Figure 4 below).

As a general summary of the data, we can state that the PSD decreases at roughly the same rate after the sunset peak, with a decay rate that fluctuates between 1.2 h and 1.6 h. This decay parameter is largely independent of frequency, and agrees well with the determination made by Hysell and Kelley (1997). This being stated, there are intriguing small variations in the spectral slope and decay rate as a function of frequency. These will be discussed in the next section.

## 4 Discussion

Figure 4 offers a different way to present our results by displaying the decay rates,  $\tau$ , as a function of wavenumber  $k = 2\pi/L = 2\pi f/(v_{sc} \sin \alpha)$  for all frequencies  $f$ . We remind the reader that  $v_{sc} \sin \alpha$  denotes the component of the spacecraft velocity that is perpendicular to the geomagnetic field and that  $L$  is the spatial scale of irregularities. The thick green (absolute density) and blue (density contrast) lines give the post-sunset structure lifetimes, with shaded regions denoting the 95 percentile error margins of the underlying exponential fits. There is a tendency for faster decay times at intermediate frequencies and a longer decay time at the highest frequency (500 m scale), that also matches the decay of the largest structures. While real, it can be seen that the decay rate differences remain small, with less than a 20% excursion between extremes in spite of a frequency range that changes by nearly *two orders of magnitude*.

To illustrate the scale-dependent response in decay times that would be associated with ambipolar diffusion we also show the plasma diffusion lifetime based on the equation

$$\tau(k) = (k^2 D_a)^{-1}, \quad (8)$$

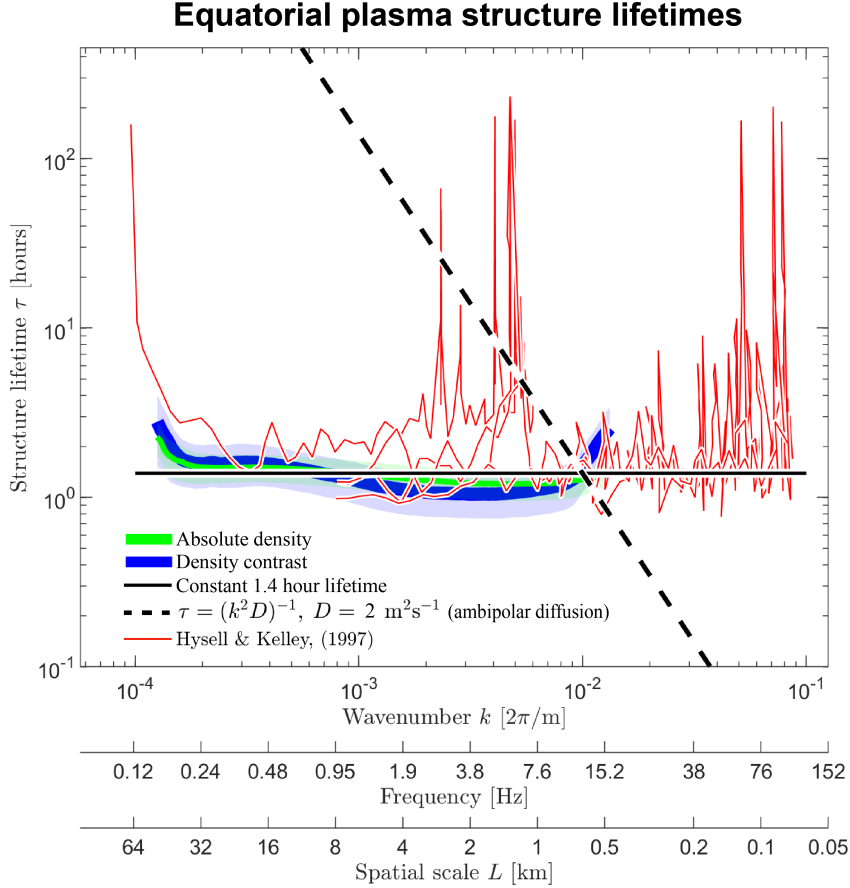


**Figure 4.** Exponential decay in all frequencies post-sunset (green and blue). Shaded blue and green areas indicate the 95-percent confidence intervals of the exponential fits. The results from Hysell and Kelley (1997) are plotted with four, thin red lines, representing four different measurements from the AE-E satellite. A power law fit (Eq. 8) is shown in thick dashed black line, while a constant 1.4 h lifetime is shown with a thick black line. The jump made by the blue curve at around 500 m scale-size could be due to noise, since the absolute plasma density (the denominator in Eq. 5) pre-sunrise is extremely low).

271 where  $D_a$  is the ambipolar diffusion coefficient that can be found for example in Vickrey  
 272 and Kelley (1982) and can be approximated with the formula

$$D_a = \frac{K_b T_e}{m_i} \frac{\nu_e}{\Omega_e \Omega_i}, \quad (9)$$

273 where  $K_b$  is the Boltzman constant,  $T_e$  is the electron temperature,  $m_i$  the ion mass,  $\nu_e$   
 274 the electron collision frequency and  $\Omega_e$  and  $\Omega_i$  are the electron and ion gyrofrequencies  
 275 respectively (Moisan & Pelletier, 2012). Eq. (8) is plotted with a thick dashed black line  
 276 in Figure 4. In stark contrast, a thick solid black line shows a constant decay rate of 1.4 hours.  
 277 Lastly, four thin red lines give the structure lifetimes estimated by Hysell and Kelley (1997),  
 278 for four different iterations by the instrumentation on board the AE-E satellite. Notably,  
 279 comparing the green and blue data with the thin red lines in Figure 4), the statistical  
 280 results of the present paper are entirely consistent with the estimates by Hysell and Kel-  
 281 ley (1997), with a decay rate of around 1.4 h for a similar satellite altitude as that of the  
 282 AE-E satellite.

As pointed out by Hysell and Kelley (1997), a scale-independent decay post-sunset implies that equatorial plasma irregularities (for the most part bubbles) decay with the stochastic description of their structures intact. This will happen if cascading, through mode-coupling, transfers energy from larger scales to smaller ones, scales that then transfer energy to even smaller scales. If the structures decay all at the same rate, this means that the energy received at one scale is transferred back to the next scale at the same rate as it comes in. In that case, Hysell and Kelley (1997) have shown that the decay rate,  $\tau$ , of previously excited structures has to be given by the condition

$$\tau \sum_{\mathbf{k}} |n_{\mathbf{k}}|^2 = D \sum_{\mathbf{k}} k^2 |n_{\mathbf{k}}|^2 \quad (10)$$

Using an ingenious heuristic model of turbulence, Hysell and Kelley (1997) have then found that the diffusion coefficient was approximately given by

$$D = \tau \frac{\ln(2k_1/k_0)}{k_1 k_2} \quad (11)$$

where the various  $k_i$  were associated with important wavelength regimes and  $\tau$  was the observed decay rate of the structures. The intriguing part of this result was that the diffusion coefficient thus inferred was essentially the ambipolar diffusion coefficient for the altitude under consideration.

The retrieval of a local ambipolar diffusion coefficient may not be coincidental. Our argument as to why the local ambipolar diffusion is recovered is as follows: the large structures give energy to the next smaller structures at a given rate, and cascading carries this transfer of information down to a scale where ambipolar diffusion will become *more rapid* than the rate at which the structures receive energy through turbulent cascade. The onset of this rapid diffusion will determine the end point of the cascading as well as the rate at which the overall structures decay over the cascading interval. Although convincing, this description, with the quoted numbers, is generalized and not specific to case studies; Hysell and Kelley (1997)'s spectra exhibited scale-independent decay down to 80 m (red data in Figure 4).

## 5 Conclusion

We have analyzed some 25,000 equatorial crossings made by the Swarm A satellite during roughly ten years of operation, and applied a PSD analysis to the Swarm Advanced Plasma Density dataset. We have aggregated the power spectra, sorting by solar local time and frequency, before adjusting the instrument's sampling frequency by the (3D) angle between spacecraft velocity and ambient magnetic field lines (see Eqs. 2–4 and Figure 2).

Figures 3 and 4 show that, after the sunset production peak, equatorial density irregularities tend to decay with a characteristic lifetime that is largely independent of spatial scale, and in line with the only previous estimate (Hysell & Kelley, 1997).

A constant and regular structure lifetime of around 1.4 hours for equatorial plasma irregularities may have important consequences for research into climatological models for the purposes of space weather forecasting, with the overarching goal of mitigating the adverse effects of radio scintillations. After all, the decay rate regulates the degree to which irregularities proliferate during the equatorial night. For scales reaching up to 75 km, no wavevector gains more power than it receives until the local ambipolar diffusion rate is obtained. That rate evaluated for structures near the end of the turbulent cascade is what determines the rate at which the entire turbulent structure decays. This is in stark contrast with the classical ambipolar diffusion regime, which depends very strongly on spatial scales.

327 The relatively slow rate at which chemical recombination proceeds (Su et al., 2006)  
 328 is exceeded by turbulent cascade, and so we expect chemical recombination rates not to  
 329 be valid for the dissipation of < 75 km turbulence present in equatorial plasma bubbles.  
 330 Large-scale models typically do not resolve this turbulence, and rely on instability growth  
 331 rates when predicting climatologies. For the same reason, such models typically rely on  
 332 decay rates that are based on expectations for chemical recombination. Our study pro-  
 333 vides a useful correction to this practice, offering a stepping stone to bridge the gap be-  
 334 tween observations (of turbulence) and the treatment of turbulent phenomena by large-  
 335 scale modeling efforts.

## 336 Open Research

337 Data from the European Space Agency’s Swarm mission can accessed at  
 338 <https://swarm-diss.eo.esa.int/>

## 339 Acknowledgments

340 This work is a part of LIPS (the Lifetimes of Ionospheric Plasma Structures) project at  
 341 the University of Oslo, and is supported in part by Research Council of Norway (RCN)  
 342 grant 324859. The authors are grateful to L Clausen, H. Kil, and V. Eccles. YJ acknowl-  
 343 edges funding from the European Research Council (ERC) under the European Union’s  
 344 Horizon 2020 research and innovation programme (ERC Consolidator Grant agreement  
 345 No. 866357, POLAR-4DSpace). Part of this research has been performed under the 4DSpace  
 346 Strategic Research Initiative at the University of Oslo.

## 347 References

- 348 Alken, P., Thébault, E., Beggan, C. D., Amit, H., Aubert, J., Baerenzung, J., . . .  
 349 Zhou, B. (2021, February). International Geomagnetic Reference Field:  
 350 the thirteenth generation. *Earth, Planets and Space*, *73*(1), 49. Retrieved  
 351 2024-01-17, from <https://doi.org/10.1186/s40623-020-01288-x> doi:  
 352 10.1186/s40623-020-01288-x
- 353 Basu, S., & Basu, S. (1985). Equatorial scintillations: Advances since ISEA-6. *Jour-  
 354 nal of atmospheric and terrestrial physics*, *47*(8-10), 753–768. (Publisher: Else-  
 355 vier)
- 356 Borovsky, J. E. (2012). Looking for evidence of mixing in the so-  
 357 lar wind from 0.31 to 0.98 AU. *Journal of Geophysical Research:  
 358 Space Physics*, *117*(A6). Retrieved 2022-04-29, from [http://  
 359 onlinelibrary.wiley.com/doi/abs/10.1029/2012JA017525](http://onlinelibrary.wiley.com/doi/abs/10.1029/2012JA017525) (eprint:  
 360 <https://agupubs.onlinelibrary.wiley.com/doi/pdf/10.1029/2012JA017525>) doi:  
 361 10.1029/2012JA017525
- 362 Dyson, P. L., McClure, J. P., & Hanson, W. B. (1974, April). In situ measure-  
 363 ments of the spectral characteristics of F region ionospheric irregularities.  
 364 *Journal of Geophysical Research*, *79*(10), 1497–1502. Retrieved 2018-10-  
 365 01, from [https://agupubs.onlinelibrary.wiley.com/doi/abs/10.1029/  
 366 JA079i010p01497](https://agupubs.onlinelibrary.wiley.com/doi/abs/10.1029/JA079i010p01497) doi: 10.1029/JA079i010p01497
- 367 Eccles, J. V., St. Maurice, J. P., & Schunk, R. W. (2015). Mechanisms  
 368 underlying the prereversal enhancement of the vertical plasma drift in  
 369 the low-latitude ionosphere. *Journal of Geophysical Research: Space  
 370 Physics*, *120*(6), 4950–4970. Retrieved 2024-02-12, from [https://  
 371 onlinelibrary.wiley.com/doi/abs/10.1002/2014JA020664](https://onlinelibrary.wiley.com/doi/abs/10.1002/2014JA020664) (eprint:  
 372 <https://agupubs.onlinelibrary.wiley.com/doi/pdf/10.1002/2014JA020664>) doi:  
 373 10.1002/2014JA020664
- 374 Fejer, B. G., Farley, D. T., Gonzales, C. A., Woodman, R. F., & Calderon, C.  
 375 (1981). F region east-west drifts at Jicamarca. *Journal of Geophysical Re-*

- 376 search: *Space Physics*, 86(A1), 215–218. Retrieved 2022-06-29, from [http://](http://onlinelibrary.wiley.com/doi/abs/10.1029/JA086iA01p00215)  
 377 [onlinelibrary.wiley.com/doi/abs/10.1029/JA086iA01p00215](http://onlinelibrary.wiley.com/doi/abs/10.1029/JA086iA01p00215) (\_eprint:  
 378 <https://agupubs.onlinelibrary.wiley.com/doi/pdf/10.1029/JA086iA01p00215>)  
 379 doi: 10.1029/JA086iA01p00215
- 380 Friis-Christensen, E., Lühr, H., & Hulot, G. (2006, April). Swarm: A constel-  
 381 lation to study the Earth’s magnetic field. *Earth, Planets and Space*, 58,  
 382 BF03351933. doi: 10.1186/BF03351933
- 383 Hapgood, M. A. (1992, May). Space physics coordinate transformations: A  
 384 user guide. *Planetary and Space Science*, 40(5), 711–717. Retrieved 2024-  
 385 01-17, from [https://www.sciencedirect.com/science/article/pii/](https://www.sciencedirect.com/science/article/pii/S003206339290012D)  
 386 003206339290012D doi: 10.1016/0032-0633(92)90012-D
- 387 Heelis, R. A. (2004, July). Electrodynamics in the low and middle latitude  
 388 ionosphere: a tutorial. *Journal of Atmospheric and Solar-Terrestrial*  
 389 *Physics*, 66(10), 825–838. Retrieved 2020-10-06, from [http://www](http://www.sciencedirect.com/science/article/pii/S1364682604000525)  
 390 [.sciencedirect.com/science/article/pii/S1364682604000525](http://www.sciencedirect.com/science/article/pii/S1364682604000525) doi:  
 391 10.1016/j.jastp.2004.01.034
- 392 Hysell, D. L., & Kelley, M. C. (1997). Decaying equatorial F region  
 393 plasma depletions. *Journal of Geophysical Research: Space Physics*,  
 394 102(A9), 20007–20017. Retrieved 2021-01-30, from [http://agupubs](http://agupubs.onlinelibrary.wiley.com/doi/abs/10.1029/97JA01725)  
 395 [.onlinelibrary.wiley.com/doi/abs/10.1029/97JA01725](http://agupubs.onlinelibrary.wiley.com/doi/abs/10.1029/97JA01725) (\_eprint:  
 396 <https://onlinelibrary.wiley.com/doi/pdf/10.1029/97JA01725>) doi: [https://](https://doi.org/10.1029/97JA01725)  
 397 [doi.org/10.1029/97JA01725](https://doi.org/10.1029/97JA01725)
- 398 Hysell, D. L., & Kudeki, E. (2004). Collisional shear instability in the equa-  
 399 torial F region ionosphere. *Journal of Geophysical Research: Space*  
 400 *Physics*, 109(A11). Retrieved 2020-10-06, from [https://agupubs](https://agupubs.onlinelibrary.wiley.com/doi/abs/10.1029/2004JA010636)  
 401 [.onlinelibrary.wiley.com/doi/abs/10.1029/2004JA010636](https://agupubs.onlinelibrary.wiley.com/doi/abs/10.1029/2004JA010636) (\_eprint:  
 402 <https://agupubs.onlinelibrary.wiley.com/doi/pdf/10.1029/2004JA010636>) doi:  
 403 10.1029/2004JA010636
- 404 Hysell, D. L., Seyler, C. E., & Kelley, M. C. (1994). Steepened struc-  
 405 tures in equatorial spread F: 2. Theory. *Journal of Geophysical Re-*  
 406 *search: Space Physics*, 99(A5), 8841–8850. Retrieved 2021-01-30, from  
 407 <http://agupubs.onlinelibrary.wiley.com/doi/abs/10.1029/93JA02960>  
 408 (\_eprint: <https://onlinelibrary.wiley.com/doi/pdf/10.1029/93JA02960>) doi:  
 409 <https://doi.org/10.1029/93JA02960>
- 410 Ivarsen, M. F., Jin, Y., Spicher, A., & Clausen, L. B. N. (2019). Direct Evidence for  
 411 the Dissipation of Small-Scale Ionospheric Plasma Structures by a Conductive  
 412 E Region. *Journal of Geophysical Research: Space Physics*, 124(4), 2935–2942.  
 413 Retrieved 2019-09-12, from [https://agupubs.onlinelibrary.wiley.com/](https://agupubs.onlinelibrary.wiley.com/doi/abs/10.1029/2019JA026500)  
 414 [doi/abs/10.1029/2019JA026500](https://agupubs.onlinelibrary.wiley.com/doi/abs/10.1029/2019JA026500) doi: 10.1029/2019JA026500
- 415 Ivarsen, M. F., Jin, Y., Spicher, A., Miloch, W., & Clausen, L. B. N.  
 416 (2021). The Lifetimes of Plasma Structures at High Lati-  
 417 tudes. *Journal of Geophysical Research: Space Physics*, 126(2),  
 418 e2020JA028117. Retrieved 2021-02-09, from [http://agupubs](http://agupubs.onlinelibrary.wiley.com/doi/abs/10.1029/2020JA028117)  
 419 [.onlinelibrary.wiley.com/doi/abs/10.1029/2020JA028117](http://agupubs.onlinelibrary.wiley.com/doi/abs/10.1029/2020JA028117) (\_eprint:  
 420 <https://onlinelibrary.wiley.com/doi/pdf/10.1029/2020JA028117>) doi:  
 421 <https://doi.org/10.1029/2020JA028117>
- 422 Ivarsen, M. F., St-Maurice, J.-P., Jin, Y., Park, J., Miloch, W., Spicher,  
 423 A., ... Clausen, L. B. N. (2021). Steepening Plasma Density  
 424 Spectra in the Ionosphere: The Crucial Role Played by a Strong E-  
 425 Region. *Journal of Geophysical Research: Space Physics*, 126(8),  
 426 e2021JA029401. Retrieved 2021-08-18, from [http://agupubs](http://agupubs.onlinelibrary.wiley.com/doi/abs/10.1029/2021JA029401)  
 427 [.onlinelibrary.wiley.com/doi/abs/10.1029/2021JA029401](http://agupubs.onlinelibrary.wiley.com/doi/abs/10.1029/2021JA029401) (\_eprint:  
 428 <https://onlinelibrary.wiley.com/doi/pdf/10.1029/2021JA029401>) doi:  
 429 10.1029/2021JA029401
- 430 Kelley, M. C. (1989, January). Chapter 7 - Effects of Plasma Flow at High Lat-

- 431 itudes. In M. C. Kelley (Ed.), *The Earth's Ionosphere* (pp. 311–343). Aca-  
 432 demic Press. Retrieved 2021-06-29, from [https://www.sciencedirect.com/](https://www.sciencedirect.com/science/article/pii/B9780124040137500125)  
 433 [science/article/pii/B9780124040137500125](https://www.sciencedirect.com/science/article/pii/B9780124040137500125) doi: 10.1016/B978-0-12-  
 434 -404013-7.50012-5
- 435 Kelley, M. C., Makela, J. J., Paxton, L. J., Kamalabadi, F., Comberiate,  
 436 J. M., & Kil, H. (2003). The first coordinated ground- and space-  
 437 based optical observations of equatorial plasma bubbles. *Geophys-*  
 438 *ical Research Letters*, *30*(14). Retrieved 2022-07-15, from [http://](http://onlinelibrary.wiley.com/doi/abs/10.1029/2003GL017301)  
 439 [onlinelibrary.wiley.com/doi/abs/10.1029/2003GL017301](http://onlinelibrary.wiley.com/doi/abs/10.1029/2003GL017301) (\_eprint:  
 440 <https://agupubs.onlinelibrary.wiley.com/doi/pdf/10.1029/2003GL017301>) doi:  
 441 10.1029/2003GL017301
- 442 Kelley, M. C., & McClure, J. P. (1981, May). Equatorial spread-F: a review of  
 443 recent experimental results. *Journal of Atmospheric and Terrestrial Physics*,  
 444 *43*(5), 427–435. Retrieved 2020-10-06, from [http://www.sciencedirect.com/](http://www.sciencedirect.com/science/article/pii/0021916981901069)  
 445 [science/article/pii/0021916981901069](http://www.sciencedirect.com/science/article/pii/0021916981901069) doi: 10.1016/0021-9169(81)90106  
 446 -9
- 447 Kelley, M. C., Pfaff, R., Baker, K. D., Ulwick, J. C., Livingston, R., Rino, C., &  
 448 Tsunoda, R. (1982). Simultaneous rocket probe and radar measurements of  
 449 equatorial spread F—Transitional and short wavelength results. *Journal of*  
 450 *Geophysical Research: Space Physics*, *87*(A3), 1575–1588.
- 451 Kil, H. (2015). The Morphology of Equatorial Plasma Bubbles - a review. *Journal*  
 452 *of Astronomy and Space Sciences*, *32*(1), 13–19. Retrieved 2020-10-06, from  
 453 <http://koreascience.or.kr/article/JAK0201509956027427.page> (Pub-  
 454 lisher: The Korean Space Science Society) doi: 10.5140/JASS.2015.32.1.13
- 455 Kil, H., & Heelis, R. A. (1998). Equatorial density irregularity structures at in-  
 456 termediate scales and their temporal evolution. *Journal of Geophysical*  
 457 *Research: Space Physics*, *103*(A3), 3969–3981. Retrieved 2020-10-06, from  
 458 <https://agupubs.onlinelibrary.wiley.com/doi/abs/10.1029/97JA03344>  
 459 (\_eprint: <https://agupubs.onlinelibrary.wiley.com/doi/pdf/10.1029/97JA03344>)  
 460 doi: 10.1029/97JA03344
- 461 Kivanc, & Heelis, R. A. (1998, April). Spatial distribution of ionospheric plasma  
 462 and field structures in the high-latitude F region. *Journal of Geophysical Re-*  
 463 *search*, *103*, 6955–6968. Retrieved 2018-08-13, from [http://adsabs.harvard](http://adsabs.harvard.edu/abs/1998JGR...103.6955K)  
 464 [.edu/abs/1998JGR...103.6955K](http://adsabs.harvard.edu/abs/1998JGR...103.6955K) doi: 10.1029/97JA03237
- 465 Knudsen, D. J., Burchill, J. K., Buchert, S. C., Eriksson, A. I., Gill, R., Wahlund,  
 466 J.-E., ... Moffat, B. (2017, February). Thermal ion imagers and Langmuir  
 467 probes in the Swarm electric field instruments. *Journal of Geophysical Re-*  
 468 *search: Space Physics*, *122*(2), 2016JA022571. Retrieved 2018-03-07, from  
 469 <http://onlinelibrary.wiley.com/doi/10.1002/2016JA022571/abstract>  
 470 doi: 10.1002/2016JA022571
- 471 Kolmogorov, A. (1941). The Local Structure of Turbulence in Incompressible  
 472 Viscous Fluid for Very Large Reynolds' Numbers. *Akademiia Nauk SSSR Dok-*  
 473 *lady*, *30*, 301–305. Retrieved 2018-05-08, from [http://adsabs.harvard.edu/](http://adsabs.harvard.edu/abs/1941DoSSR...30...301K)  
 474 [abs/1941DoSSR...30...301K](http://adsabs.harvard.edu/abs/1941DoSSR...30...301K)
- 475 LaBelle, J., Kelley, M. C., & Seyler, C. E. (1986). An analysis of the role of drift  
 476 waves in equatorial spread F. *Journal of Geophysical Research: Space Physics*,  
 477 *91*(A5), 5513–5525. (Publisher: Wiley Online Library)
- 478 Le, G., Huang, C.-S., Pfaff, R. F., Su, S.-Y., Yeh, H.-C., Heelis, R. A., ... Hairston,  
 479 M. (2003). Plasma density enhancements associated with equatorial spread  
 480 F: ROCSAT-1 and DMSP observations. *Journal of Geophysical Research:*  
 481 *Space Physics*, *108*(A8). Retrieved 2020-10-06, from [https://agupubs](https://agupubs.onlinelibrary.wiley.com/doi/abs/10.1029/2002JA009592)  
 482 [.onlinelibrary.wiley.com/doi/abs/10.1029/2002JA009592](https://agupubs.onlinelibrary.wiley.com/doi/abs/10.1029/2002JA009592) (\_eprint:  
 483 <https://agupubs.onlinelibrary.wiley.com/doi/pdf/10.1029/2002JA009592>) doi:  
 484 10.1029/2002JA009592
- 485 Moisan, M., & Pelletier, J. (2012). Hydrodynamic Description of a Plasma. In

- 486 M. Moisan & J. Pelletier (Eds.), *Physics of Collisional Plasmas: Introduction*  
 487 *to High-Frequency Discharges* (pp. 203–335). Dordrecht: Springer Netherlands.  
 488 Retrieved 2019-09-02, from [https://doi.org/10.1007/978-94-007-4558-2\\_3](https://doi.org/10.1007/978-94-007-4558-2_3)  
 489 doi: 10.1007/978-94-007-4558-2\_3
- 490 Mounir, H., Berthelier, A., Cerisier, J. C., Lagoutte, D., & Beghin, C. (1991,  
 491 November). The small-scale turbulent structure of the high latitude ionosphere  
 492 - Arcad-Aureol-3 observations. *Annales Geophysicae*, 9, 725–737. Retrieved  
 493 2018-03-07, from <http://adsabs.harvard.edu/abs/1991AnGeo...9..725M>
- 494 Nakanishi, K., Iyemori, T., Taira, K., & Lühr, H. (2014, May). Global and fre-  
 495 quent appearance of small spatial scale field-aligned currents possibly driven  
 496 by the lower atmospheric phenomena as observed by the CHAMP satellite  
 497 in middle and low latitudes. *Earth, Planets and Space*, 66(1), 40. Re-  
 498 trieved 2022-06-30, from <https://doi.org/10.1186/1880-5981-66-40> doi:  
 499 10.1186/1880-5981-66-40
- 500 Oya, H., Takahashi, T., & Watanabe, S. (1986). Observation of Low Latitude Iono-  
 501 sphere by the Impedance Probe on Board the Hinotori Satellite. *Journal of ge-*  
 502 *omagnetism and geoelectricity*, 38(2), 111–123. doi: 10.5636/jgg.38.111
- 503 Park, J., Min, K. W., Lee, J.-J., Kil, H., Kim, V. P., Kim, H.-J., ... Lee,  
 504 D. Y. (2003). Plasma blob events observed by KOMPSAT-1 and DMSP  
 505 F15 in the low latitude nighttime upper ionosphere. *Geophysical Re-*  
 506 *search Letters*, 30(21). Retrieved 2020-10-06, from [https://agupubs](https://agupubs.onlinelibrary.wiley.com/doi/abs/10.1029/2003GL018249)  
 507 [.onlinelibrary.wiley.com/doi/abs/10.1029/2003GL018249](https://agupubs.onlinelibrary.wiley.com/doi/abs/10.1029/2003GL018249) (\_eprint:  
 508 <https://agupubs.onlinelibrary.wiley.com/doi/pdf/10.1029/2003GL018249>) doi:  
 509 10.1029/2003GL018249
- 510 Purslow, B. W. (1958, January). Ionospheric Drift in the F2 Region near the Mag-  
 511 netic Equator. *Nature*, 181(4601), 35–36. Retrieved 2022-06-29, from [http://](http://www.nature.com/articles/181035a0)  
 512 [www.nature.com/articles/181035a0](http://www.nature.com/articles/181035a0) (Number: 4601 Publisher: Nature Pub-  
 513 lishing Group) doi: 10.1038/181035a0
- 514 Rino, C. L., Carrano, C. S., Groves, K. M., & Roddy, P. A. (2016). A characteriza-  
 515 tion of intermediate-scale spread F structure from four years of high-resolution  
 516 C/NOFS satellite data. *Radio Science*, 51(6), 779–788. (Publisher: AGU)
- 517 Rino, C. L., Tsunoda, R. T., Petriceks, J., Livingston, R. C., Kelley, M. C.,  
 518 & Baker, K. D. (1981). Simultaneous rocket-borne beacon and  
 519 in situ measurements of equatorial spread F—Intermediate wave-  
 520 length results. *Journal of Geophysical Research: Space Physics*,  
 521 86(A4), 2411–2420. Retrieved 2020-10-06, from [https://agupubs](https://agupubs.onlinelibrary.wiley.com/doi/abs/10.1029/JA086iA04p02411)  
 522 [.onlinelibrary.wiley.com/doi/abs/10.1029/JA086iA04p02411](https://agupubs.onlinelibrary.wiley.com/doi/abs/10.1029/JA086iA04p02411) (\_eprint:  
 523 <https://agupubs.onlinelibrary.wiley.com/doi/pdf/10.1029/JA086iA04p02411>)  
 524 doi: 10.1029/JA086iA04p02411
- 525 Skinner, N. J., Hope, J., & Wright, R. W. (1958, November). Horizontal Drift Mea-  
 526 surements in the Ionosphere near the Equator. *Nature*, 182(4646), 1363–1365.  
 527 Retrieved 2022-06-29, from <http://www.nature.com/articles/1821363a0>  
 528 (Number: 4646 Publisher: Nature Publishing Group) doi: 10.1038/1821363a0
- 529 Song, H., Park, J., Buchert, S., Jin, Y., Chao, C. K., Lee, J., & Yi, Y.  
 530 (2022). A Small Peak in the Swarm-LP Plasma Density Data at  
 531 the Dayside Dip Equator. *Journal of Geophysical Research: Space*  
 532 *Physics*, 127(7), e2022JA030319. Retrieved 2024-01-05, from [https://](https://onlinelibrary.wiley.com/doi/abs/10.1029/2022JA030319)  
 533 [onlinelibrary.wiley.com/doi/abs/10.1029/2022JA030319](https://onlinelibrary.wiley.com/doi/abs/10.1029/2022JA030319) (\_eprint:  
 534 <https://onlinelibrary.wiley.com/doi/pdf/10.1029/2022JA030319>) doi:  
 535 10.1029/2022JA030319
- 536 Stoica, P., & Moses, R. L. (2005). *Spectral Analysis of Signals*. Pearson Prentice  
 537 Hall. (Google-Books-ID: h78ZAQAIAAJ)
- 538 Su, S.-Y., Liu, C. H., Ho, H. H., & Chao, C. K. (2006). Distribution  
 539 characteristics of topside ionospheric density irregularities: Equato-  
 540 rial versus midlatitude regions. *Journal of Geophysical Research:*

- 541 *Space Physics*, 111(A6). Retrieved 2024-03-07, from [https://](https://onlinelibrary.wiley.com/doi/abs/10.1029/2005JA011330)  
542 [onlinelibrary.wiley.com/doi/abs/10.1029/2005JA011330](https://onlinelibrary.wiley.com/doi/abs/10.1029/2005JA011330) (\_eprint:  
543 <https://agupubs.onlinelibrary.wiley.com/doi/pdf/10.1029/2005JA011330>) doi:  
544 10.1029/2005JA011330
- 545 Tröbs, M., & Heinzl, G. (2006, February). Improved spectrum estimation from dig-  
546 itized time series on a logarithmic frequency axis. *Measurement*, 39(2), 120–  
547 129. Retrieved 2018-03-06, from [http://www.sciencedirect.com/science/](http://www.sciencedirect.com/science/article/pii/S026322410500117X)  
548 [article/pii/S026322410500117X](http://www.sciencedirect.com/science/article/pii/S026322410500117X) doi: 10.1016/j.measurement.2005.10.010
- 549 Vickrey, J. F., & Kelley, M. C. (1982, June). The effects of a conducting E layer on  
550 classical F region cross-field plasma diffusion. *Journal of Geophysical Research:*  
551 *Space Physics*, 87(A6), 4461–4468. Retrieved 2018-03-06, from [http://](http://onlinelibrary.wiley.com/doi/10.1029/JA087iA06p04461/abstract)  
552 [onlinelibrary.wiley.com/doi/10.1029/JA087iA06p04461/abstract](http://onlinelibrary.wiley.com/doi/10.1029/JA087iA06p04461/abstract) doi:  
553 10.1029/JA087iA06p04461
- 554 Woodman, R. F. (1972). East-west ionospheric drifts at the magnetic equator. *un-*  
555 *defined*. Retrieved 2022-06-29, from [https://www.semanticscholar.org/](https://www.semanticscholar.org/paper/East-west-ionospheric-drifts-at-the-magnetic-Woodman/5c3b012a8a68019199019ca2f8d7452e7d9fd74c)  
556 [paper/East-west-ionospheric-drifts-at-the-magnetic-Woodman/](https://www.semanticscholar.org/paper/East-west-ionospheric-drifts-at-the-magnetic-Woodman/5c3b012a8a68019199019ca2f8d7452e7d9fd74c)  
557 [5c3b012a8a68019199019ca2f8d7452e7d9fd74c](https://www.semanticscholar.org/paper/East-west-ionospheric-drifts-at-the-magnetic-Woodman/5c3b012a8a68019199019ca2f8d7452e7d9fd74c)
- 558 Woodman, R. F., & Hoz, C. L. (1976). Radar observations of F region  
559 equatorial irregularities. *Journal of Geophysical Research (1896-1977)*,  
560 81(31), 5447–5466. Retrieved 2020-10-06, from [https://agupubs](https://agupubs.onlinelibrary.wiley.com/doi/abs/10.1029/JA081i031p05447)  
561 [.onlinelibrary.wiley.com/doi/abs/10.1029/JA081i031p05447](https://agupubs.onlinelibrary.wiley.com/doi/abs/10.1029/JA081i031p05447) (\_eprint:  
562 <https://agupubs.onlinelibrary.wiley.com/doi/pdf/10.1029/JA081i031p05447>)  
563 doi: 10.1029/JA081i031p05447
- 564 Yeh, K. C., & Liu, C.-H. (1982, April). Radio wave scintillations in the ionosphere.  
565 *IEEE Proceedings*, 70, 324–360. Retrieved 2018-05-08, from [http://adsabs](http://adsabs.harvard.edu/abs/1982IEEEP..70..324Y)  
566 [.harvard.edu/abs/1982IEEEP..70..324Y](http://adsabs.harvard.edu/abs/1982IEEEP..70..324Y)